第 43 卷 第 24 期/2023 年 12 月/光学学报 封面文章·研究论文

光学学报

激光雷达比历史数据的模糊综合评价研究

胡先哲[1,2]，刘东[1,2,3,4*]，肖达[1]，张凯[1]，毕磊[5]，张敬昕[1]，李蔚泽[1]，李晓涛[1]，邓洁松[1]，周雨迪[1,6]，刘群[1,6]，吴兰[1]，刘崇[1]，万学平[7]，陈文泰[7]，陈晓龙[7]，周剑锋[7]

[1]浙江大学光电科学与工程学院极端光学技术与仪器全国重点实验室，浙江 杭州 310027；

[2]东海实验室，浙江 舟山 316021；

[3]浙江大学杭州国际科创中心，浙江 杭州 311200；

[4]浙江大学嘉兴研究院，浙江 嘉兴 314000；

[5]浙江大学地球科学学院浙江省地学大数据与地球深部资源重点实验室，浙江 杭州 310027；

[6]浙江大学宁波科创中心，浙江 宁波 315100；

[7]无锡中科光电技术有限公司，江苏 无锡 214135

摘要 气溶胶是地气系统辐射强迫评估的主要不确定来源之一，激光雷达探测的气溶胶廓线数据有助于定量评估气溶胶的气候效应。除已发布的气溶胶观测产品外，大量气溶胶激光雷达观测数据分布于文献中。然而，目前尚缺乏对气溶胶历史文献数据的整合分析。因此，聚焦现有观测产品较缺乏的激光雷达比参数，充分考虑气溶胶的类型差异，提出了一种激光雷达比历史文献数据的模糊综合评价分析方法。基于Web of Science数据库，发现不同类型气溶胶（沙尘、沙尘混合、火山灰、海洋、烟尘、城市工业气溶胶）的激光雷达比均呈高斯分布，且集中范围均存在重叠。历史文献数据能与气溶胶观测数据产品提供的数据形成互补，所提出的模糊综合评价分析方法有助于提升人们对气溶胶光学特性的认识。

关键词 气溶胶；激光雷达比；历史数据；模糊综合评价

中图分类号 P407 **文献标志码** A **DOI**：10.3788/AOS231150

1 引 言

大气气溶胶是悬浮在空气中的微小颗粒，对气候和辐射强迫有着重要的影响[1-2]。气溶胶存在显著的时间和空间分布差异，是地球气候以及辐射强迫评估中主要的不确定来源之一[3-4]。了解气溶胶的时空分布及其演变规律是定量研究气溶胶对气候、环境影响的基础[5]。气溶胶的时空差异与气溶胶的源头、输运、沉降和清除过程相关。气溶胶的来源或排放机制决定了其类型[6]，确定气溶胶的类型有助于研究人员对气溶胶进行溯源。

激光雷达作为一种主动式光学遥感设备，能够探测气溶胶的垂直分布及快速变化[5-7]。米散射激光雷达由于结构简单且成本较低，被最早应用于大气气溶胶的探测，但它存在“一个方程，两个未知数”的欠定问题[8-9]。为此，Fernald[10]首次提出将激光雷达比（气溶胶消光系数与后向散射系数的比值）假设为定值。结合单次散射反照率以及散射相函数的定义，激光雷达比的值仅与粒子的单次散射反照率以及粒子在180°散射角处的相函数相关[11]。单次散射反照率反映了气溶胶的吸收特性；散射相函数与粒子的形状和大小紧密相关。因此，气溶胶的激光雷达比值仅取决于气溶胶的粒子形态、粒径分布、复折射率等，而与气溶胶含量无关[12-13]。Ackermann[12]通过数值模拟发现，不同类型气溶胶的激光雷达比并不相同。

目前，国内外已经开展了大量有关气溶胶特性的激光雷达观测与研究，积累了大量宝贵的观测资料，取得了众多有价值的成果。其中，气溶胶探测网络和星载激光雷达均能提供气溶胶的历史观测数据产品[14-15]。但是各研究单位和厂商开发的气溶胶探测网络和星载激光雷达的设计思想、设计结构、反演方法等不统一，导致不同来源的激光雷达数据的存储格式不统一，数据质量参差不齐，缺乏一致性和可比性，难以形成共识性的结论[16-17]。且现有的激光雷达大多为米散射激光雷达[18-19]，并不能提供气溶胶激光雷达比的观测数据。期刊文献中也保存了大量关于气溶胶光学

收稿日期：2023-06-16；**修回日期**：2023-08-03；**录用日期**：2023-08-11；**网络首发日期**：2023-08-21

基金项目：国家重点研发计划（2022YFB3901704，2022YFC2203904，2021YFC2202001）、中央引导地方科技发展资金项目（2022ZYYDSAA00273）、国家自然科学基金（62205289）、浙江省自然科学基金（LQ23F050011）

通信作者：*liudongopt@zju.edu.cn

特性的历史数据，其中包含了气溶胶的类型判别结果以及该类型气溶胶的激光雷达比范围。这些文献结论清晰，易于分析，但不同研究对气溶胶类型的定义并不统一，相同类型气溶胶的激光雷达比范围存在差异，历史文献数据分布比较分散，且未见专门针对气溶胶历史文献数据的分析方法。

本文以气溶胶激光雷达比作为研究对象，首先以模糊评价的方式提出对气溶胶激光雷达比历史文献数据的分析方法，构造了置信度这一模糊评价指标；然后以 Web of Science 核心合集数据库中的历史文献数据为例，总结分析了不同类型气溶胶的历史数据分布；最后以数据代表性、可靠性、影响力三个评价因子对所检索的历史文献数据展开模糊综合评价分析，给出了不同类型气溶胶激光雷达比置信度的分布情况以及集中范围。研究结果为 Fernald 法中激光雷达比的假设以及气溶胶分类提供了依据和参考，对气溶胶特性以及其辐射效应的研究有重要意义。

2　方　　法

气溶胶激光雷达比的历史文献数据包含了气溶胶类型的判别结果以及该类型气溶胶激光雷达比的范围。但由于不同历史数据的来源不同，数据信息在测量时长以及测量仪器的种类等方面存在较大的差异，因此在进行分析时，有必要引入一个评价指标为不同的历史数据赋予不同的权重。

模糊综合评价是模糊学中最为基础的评价方法，被广泛地应用于环境、气象预报等诸多领域[20]。不同类型气溶胶的激光雷达比没有明确的边界范围，存在一定的模糊性。基于模糊综合评价的思想，提出针对气溶胶激光雷达比历史文献数据的模糊综合评价分析方法，设计了历史数据置信度(confidence level)这一评价指标，同时结合历史数据的来源、测量时长、仪器种类等评价因子，衡量不同历史数据的参考权重，以便进一步分析各类型气溶胶激光雷达比的数值分布情况。

气溶胶激光雷达比的历史数据置信度分析流程如图 1 所示。首先，选择 n 个气溶胶激光雷达比历史数据的评价因子，利用层次分析法(AHP)[20]确定每个评价因子对置信度的贡献度占比。具体步骤为：1)构造判断矩阵 $\boldsymbol{A}=\left(a_{ij}\right)_{n\times n}$，其中 a_{ij} 是第 i 个评价因子相对于第 j 个评价因子的重要性程度，a_{ij} 数值越高，前者比后者越重要，$a_{ii}=1$ 且 $a_{ij}=1/a_{ji}$；2)根据 $\boldsymbol{AW}=\lambda_{\max}\boldsymbol{W}$ 计算得到贡献度权重向量 $\boldsymbol{W}=\left(w_i\right)_{1\times n}$ 以及特征值 $\lambda_{\max}$；3)计算一致性指标 $V_{\mathrm{C.I.}}=\left(\lambda_{\max}-n\right)/\left(n-1\right)$，根据表 1 得到 $V_{\mathrm{R.I.}}$，再计算一致性比例 $V_{\mathrm{C.R.}}=V_{\mathrm{C.I.}}/V_{\mathrm{R.I.}}$，若 $V_{\mathrm{C.R.}}<0.1$，则认为判断矩阵的一致性是可以接受的，否则需要对判断矩阵进行修正。

其次，根据评价因子的特点，确定每个历史数据评价因子的隶属函数(membership function)μ。结合权重向量 $\boldsymbol{W}$ 计算多个评价因子的气溶胶激光雷达比历史数据的置信值(confidence value)C_{V}，表示为

$$C_{\mathrm{V}}=\sum_{i=1}^{n}w_i\mu_i,\tag{1}$$

式中，w_i 和 μ_i 分别为第 i 项评价因子的置信值贡献度权重以及隶属函数输出值。

最后，在对所有历史数据均进行置信值计算后，对相同类型、相同波长的历史数据(historical data)进行累加(accumulate)处理，从而得到该类型、该波长下激光雷达比的总置信值(total confidence value)$C_{\mathrm{V,total}}$ 的分布。由于总置信值受历史数据量的影响，为方便历史数据的综合对比评价，对总置信值进行归一化处理，从而得到不同类型气溶胶激光雷达比历史数据置信度 C_{L} 的分布情况。

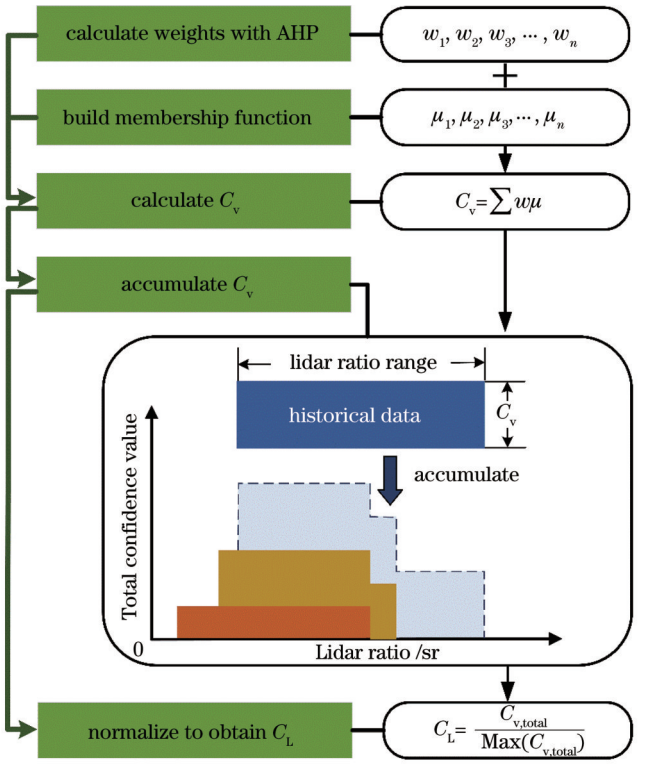

图 1　气溶胶激光雷达比历史数据置信度分析示意图

Fig. 1　Schematic diagram of the confidence level analysis of historical aerosol lidar ratio data

表 1　不同矩阵阶数 n 的 $V_{\mathrm{R.I.}}$ 值

Table 1　$V_{\mathrm{R.I.}}$ with different matrix order n

n	1	2	3	4	5	6	7	8	9	10
$V_{\mathrm{R.I.}}$	0	0	0.51	0.89	1.12	1.25	1.35	1.42	1.46	1.49

3　数　　据

基于 Web of Science 核心合集数据库，以关键词“激光雷达比(lidar ratio)”和“消光后向散射比(extinction-to-backscatter ratio)”检索获取 2022 年以前的研究成果。选取保留包含气溶胶类型判别结果的激光雷达比实测数据文献。由于 Web of Science 数据库

的检索关键词局限于标题和摘要，因此，分析结果并未完全覆盖 Web of Science 数据库中所有的历史文献数据。

在进行分析前，首先需要确定本研究包含的气溶胶类型。气溶胶通常为混合状态，很少存在纯气溶胶类型的理想状态[21]，因此，基于不同的仪器特点[17,22]，气溶胶类型的定义方式存在诸多不同。沙尘气溶胶或者海洋气溶胶由于其来源的特殊性，容易与其他气溶胶区分，因此常见于各种气溶胶分类中，如：Omar 等[23]定义了沙尘、污染沙尘、清洁大陆、污染大陆、清洁海洋和烟尘等 6 种气溶胶类型。Levy 等[24]则根据气溶胶的粒子形态和吸收强弱将气溶胶分为球形气溶胶（非吸收型、适度吸收型、吸收型）和非球形气溶胶。在 AERONET(aerosol robotic network)气溶胶测量分析中，Dubovik 等[6]将气溶胶分为沙尘、生物质燃烧、城市工业和海洋等 4 种主要类型；Burton 等[25]根据机载高光谱分辨率激光雷达（HSRL）获得的数据定义了 8 种气溶胶类型，包括烟尘、新鲜烟尘、城市、污染海洋、海洋、沙尘混合、纯沙尘和冰云气溶胶。不同的研究对沙尘混合气溶胶的定义也并不相同，在 Omar 等[23]的研究中，沙尘混合气溶胶被定义为沙尘和生物质燃烧烟尘的混合物[23]，而 Wang 等[26]则将其定义为城市气溶胶和沙尘气溶胶的混合物。本研究参考 Burton 等[25]的定义，将沙尘气溶胶与其他类型气溶胶的混合物归类为沙尘混合气溶胶。由于本研究是基于激光雷达比历史数据的研究，不存在仪器的限制，因此结合检索的激光雷达比历史数据结果，选择了沙尘、沙尘混合、火山灰、海洋、烟尘、城市工业气溶胶等 6 种气溶胶类型（与其他研究的分类基本保持一致）。

同一份数据来源不仅包含了气溶胶类型判别结果以及激光雷达比范围，还包含了测量仪器种类、激光波长、测量时长等与历史数据相关的其他信息。将气溶胶类型判别结果、激光波长、激光雷达比范围、测量仪器种类、测量时长、数据来源等多维信息作为一个历史数据信息单元，图 2 展示了上述 6 种类型气溶胶，包括沙尘[21,27-57]、沙尘混合[37,58-66]、火山灰[67-75]、海洋[39,48,56,58,62,76-78]、烟尘[21,44,48,56,59-61,78-91]、城市工业[21,29,45-48,56,92-99]的共 283 个激光雷达比历史数据信息单元的统计情况。

沙尘气溶胶约占全球气溶胶总质量的 1/3，全球沙尘带从非洲北部的撒哈拉沙漠一直延伸到塔克拉玛干沙漠和戈壁沙漠[100]。而且沙尘气溶胶具有较高的退偏比，便于与其他类型气溶胶区分，因此沙尘气溶胶的历史数据量远多于其他气溶胶，约占历史文献数据总量的 36%，沙尘混合气溶胶占历史文献数据总量的 10%。生物质燃烧产生的烟尘气溶胶通常包含有毒物质，且主要在对流层扩散[87]，对空气质量和人类健康构成了较大威胁。城市工业气溶胶由城市内交通、工业生产等人为活动产生，主要为细模态粒子[101]。由于烟尘气溶胶和城市工业气溶胶会对人类健康、空气质量等产生直接影响，更容易受到社会和科学界的关注，因此其历史文献数据量也相对较多，烟尘和城市工业气溶胶数据量在历史文献数据总量中的占比分别约为 25% 和 13%。火山气溶胶由火山喷发产生，具有超细模态、细模态和粗模态的多峰粒径分布[102]。由于其成分复杂，在对流层的寿命较短[103]，其历史数据量相对较少，占历史数据总量的 9%。海洋气溶胶是海盐颗粒以及浮游植物排放物的氧化产物，主要分布于海洋或临海地区[104]。由于观测地点的限制，其历史数据量少，仅占历史数据总量的 7%。

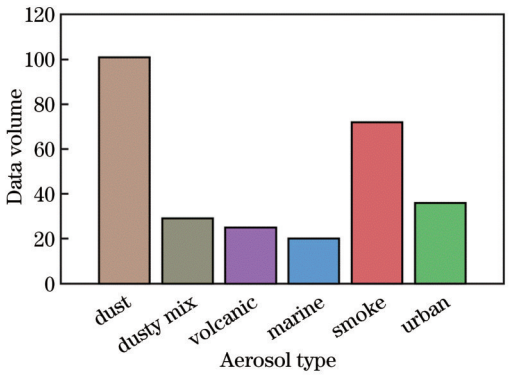

图 2　各类气溶胶激光雷达比的历史文献数据分布

Fig. 2　Historical literature data distribution of various aerosol lidar ratios

4　分析与讨论

不同历史文献数据的主要差异包括数据信息包含的测量时长、测量仪器种类以及数据来源的影响力。其中：测量时间的长短能够体现历史数据的数据量代表性；测量仪器的精度不同能够反映历史数据的数据可靠性；数据来源的影响力可以表征历史数据的认可程度。使用层次分析法时评价因子数量应不少于三个。因此，选取了历史数据的数据代表性（representativeness）、可靠性（reliability）、影响力（influence）三个指标作为评价因子，进行历史文献数据的模糊综合评价分析。

4.1　计算评价因子贡献度的权重

由于数据代表性、可靠性、影响力对历史数据置信度的贡献率不同，因此首先需要为每个评价因子赋予不同的权重。根据层次分析法确定数据代表性 w_1、可靠性 w_2、影响力 w_3 三个指标的贡献度权重（笔者认为三者按重要程度依次为数据代表性、可靠性、影响力，则 $a_{12}<a_{13}$，$a_{23}>1$ 且 $w_1>w_2>w_3$），并以此构建历史数据置信度评价指标判断矩阵，如表 2 所示。

计算得到数据代表性、可靠性、影响力的权重向量 $\boldsymbol{W}=[w_1,w_2,w_3]=[0.54,0.30,0.16]$，进而得到一致性比例 $V_{\mathrm{C.I.}}=0.0053<0.1$，满足层次分析法判断矩阵的一致性检验，说明判断矩阵设计较为合理。

表2　历史数据置信度的评价指标判断矩阵

Table 2　Evaluation index judgment matrix of historical data credibility

Evaluation indicator	Representativeness	Reliability	Influence
Representativeness	1	2	3
Reliability	1/2	1	2
Influence	1/3	1/2	1

4.2　构造评价因子的隶属度函数

4.2.1　数据代表性

气溶胶的历史数据不同于实验数据，不同来源的历史数据容量存在较大差异，一组历史数据可能代表一天、一个月或更长时间的观测结果。历史数据的数据容量越大，数据特征或统计数据的频率越稳定。Pisani 等[105]在 EARLINET(European aerosol research lidar network)的那不勒斯站点发现，不同季节沙尘天气气溶胶激光雷达比的分布存在一定差异，由此可见，一年以内的数据可能会受到季风或季节性活动的影响。Noh 等[106]在韩国 Anmyeon 岛气溶胶激光雷达比特性的研究中发现，2004 年和 2005 年相同季节观测到的气溶胶激光雷达比存在明显差异。在本次整理的历史数据中，观测时长超过 3 年的仅占所有数据的 9.2%，因此选取 3 年观测时间作为上限来表征历史数据的数据代表性。

数据代表性的隶属度函数 μ_1 为

$$\mu_1=\begin{cases} T/36, & T<36 \\ 1, & T\geqslant 36 \end{cases}, \tag{2}$$

式中，T 为测量的总月份数。

4.2.2　数据可靠性

根据陈洁[11]对激光雷达比反演方法的研究，获取激光雷达比的方法主要包括 4 类：1)地基太阳光度计反演法；2)米散射激光雷达约束反演法；3)拉曼激光雷达反演法；4)HSRL 反演法。不同的仪器在激光雷达比的反演误差上存在较大差距。Herrera 等[107]研究分析了太阳光度计 GRASP 算法对气溶胶检索特性不确定性的动态估计，结果显示，该算法反演的激光雷达比的误差范围为 20%～55%。米散射激光雷达约束反演法并不能直接反演激光雷达比，通常利用约束反演检索获得激光雷达比。以 CALIOP 激光雷达为例，其检索的激光雷达比有 30% 左右的误差[108]。拉曼激光雷达反演法先对拉曼通道信号进行微分求出消光系数，接着联合米散射通道信号和拉曼通道信号求出后向散射系数，再用两者相除得到激光雷达比，其反演误差约为 20%[109]。HSRL 反演法利用气溶胶和大气分子的散射谱谱宽差异，通过滤光器将两者分离开来，提高了气溶胶光学参数的反演精度，但未见报道明确给出其激光雷达比的反演误差。笔者曾经比较过 HSRL 反演法和拉曼激光雷达反演法的测量结果，二者的精度接近，约为 20%。因此数据的可靠性可由激光雷达比反演误差来表征，表示为

$$U_2=\begin{cases} 1-0.55, & I \text{ is sun photometer} \\ 1-0.3, & I \text{ is Mie lidar} \\ 1-0.2, & I \text{ is Raman lidar or HSRL} \end{cases}, \tag{3}$$

式中，I 为测量仪器种类。归一化后，数据可靠性的隶属度函数 μ_2 为

$$\mu_2=\begin{cases} 0.5625, & I \text{ is sun photometer} \\ 0.875, & I \text{ is Mie lidar} \\ 1, & I \text{ is Raman lidar or HSRL} \end{cases}。 \tag{4}$$

4.2.3　数据影响力

历史数据的来源包含期刊文献和会议文献两种类型。目前，衡量期刊影响力的指标较多，较具代表性的有美国科学信息研究所《期刊引证报告》(JCR)中的期刊影响因子(IF)、Elsevier 集团 Scopus 数据库的 CiteScore(CS)以及中国科学院文献情报中心 SCI(science citation index)期刊分区数据等。其中，CS 和 IF 可以对期刊的影响力进行量化评价，因此，本研究将 CS 作为数据影响力的隶属度函数分析因素。另外，会议文献主要以 EPJ Web of Conferences 为主，其 CS 为 0.9，而其他会议文献未见 CS 指标评分，因此将会议文献的数据影响力均视为 0.9。归一化后数据影响力的隶属度函数 μ_3 为

$$\mu_3=\begin{cases} C_S/C_{\mathrm{Max}}, & P \text{ is journal article} \\ 0.9/C_{\mathrm{Max}}, & P \text{ is conference papers} \end{cases}, \tag{5}$$

式中：C_S 为历史数据来源的 CS 指标评分；C_{Max} 为所有历史数据来源 CS 指标评分的最大值；P 为数据来源类型。

4.3　历史数据的置信度分析

图 3 展示了各类气溶胶激光雷达比历史数据的置信度分布曲线及其高斯拟合。每种气溶胶类型的激光雷达比置信度均表现出高斯分布，且历史数据量(N)越大，高斯拟合的拟合系数 R^2 越趋近于 1，置信度呈正态分布越明显。其中：沙尘气溶胶由于粒子尺寸偏大，光学特性的波长依赖性较小[110]，激光雷达比历史数据置信度在 355 nm 和 532 nm 波长处的分布基本一致；污染沙尘气溶胶受沙尘气溶胶的影响较大，其置信度分布与沙尘气溶胶相似；海洋气溶胶的激光雷达比在 355 nm 和 532 nm 波长处均表现出不同于其他气溶胶的低值，且 532 nm 波长处的激光雷达比置信度的高斯拟合效果不佳，这可能是其历史数据量过少造成的。各类气溶胶激光雷达比的历史数据置信度涵盖范围较广，相互间均存在数值重叠部分，且置信度呈现高斯分布趋势。而目前传统的气溶胶类型识别方法一般采用决策树方法，即根据多种光学特性按照不同的阈值进行气溶胶类型的识别，但使用固定阈值截断气溶胶数据容易造成气溶胶类型的误识别以及置信度分布的不连续。

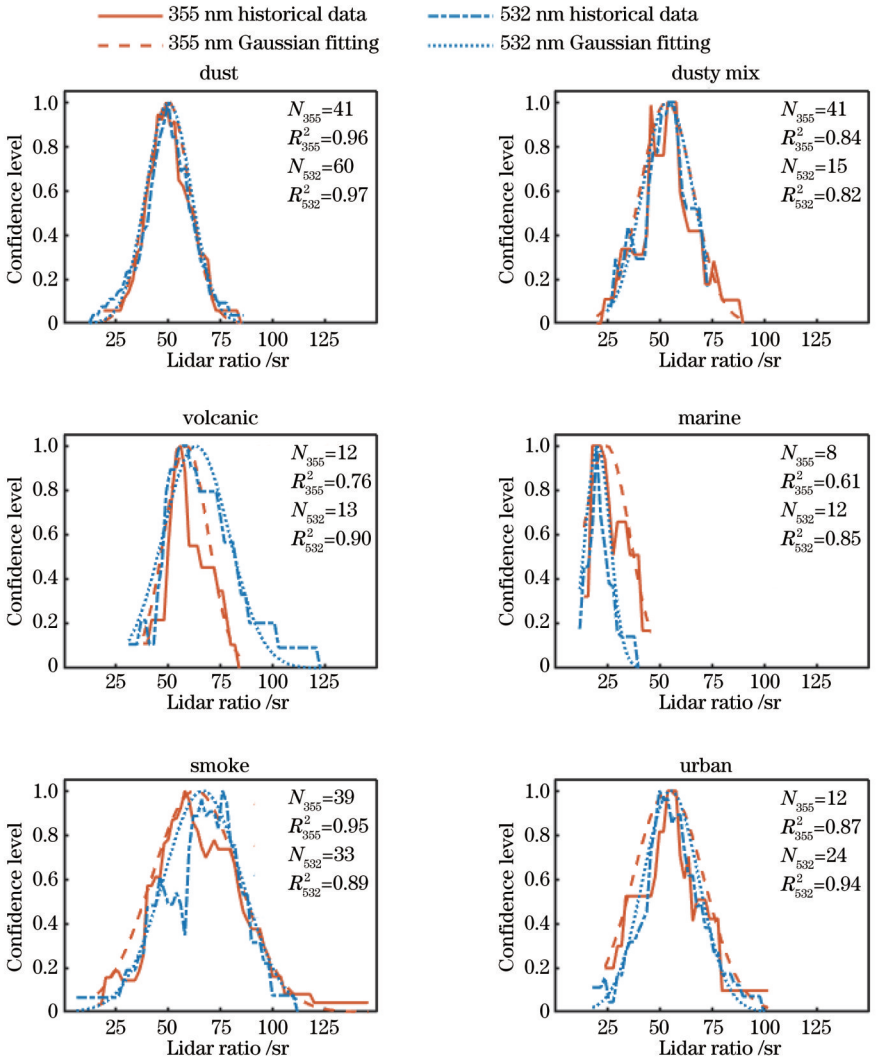

图 3　各类气溶胶激光雷达比历史数据置信度分布及其高斯拟合

Fig. 3　Confidence level distribution and its Gaussian fitting curves of historical aerosol lidar ratio data

由图 3 可知，各类气溶胶在激光雷达比分布上均表现出类似高斯分布的不同聚集趋势。图 4 展示了不同类型气溶胶在 355 nm 和 532 nm 波长处的激光雷达比历史数据置信度分布箱图。其中：烟尘气溶胶的激光雷达比相对偏高，而海洋气溶胶的则明显偏低。烟尘气溶胶的激光雷达比历史数据分布较为分散，其箱体和虚线均长于其他气溶胶，可能是燃烧物种类、位置（东欧、西伯利亚或加拿大）[80]、火灾类型的差异导致了其历史数据相对较大的分布范围[79]。从箱图的中位数也可以看出，各类气溶胶激光雷达比历史数据的置信度中位数基本位于中心位置，分布较为对称，未见明显分布偏态。

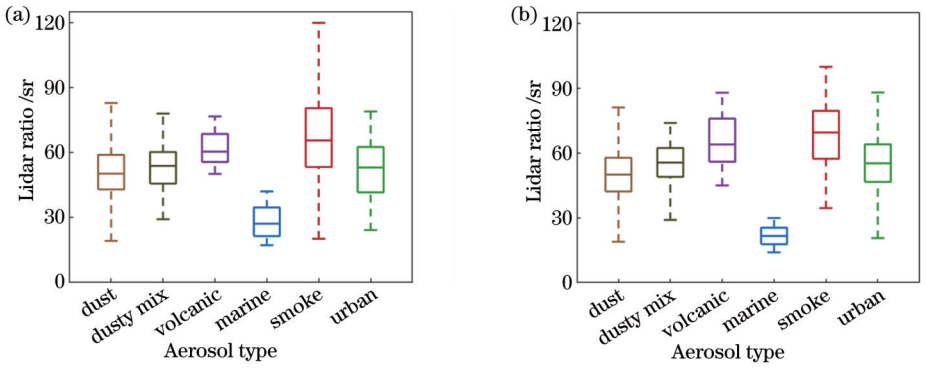

图 4　不同波长处气溶胶激光雷达比的历史数据置信度分布箱图。(a)355 nm；(b)532 nm

Fig. 4　Distribution box diagrams of confidence level of historical aerosol lidar ratio data at different wavelengths. (a) 355 nm; (b) 532 nm

不同源地的沙尘气溶胶矿物成分不同，因此其光学特性存在差异[111]。对亚洲沙尘、中东沙尘以及撒哈拉沙尘等三种不同源地的沙尘气溶胶进行上述置信度分析，图 5 展示了三种沙尘气溶胶在 355 nm 和 532 nm 波长处的激光雷达比历史数据置信度分布的箱图。三种沙尘气溶胶均表现出较小的波长依赖性。其中：撒哈拉沙尘气溶胶在 355 nm 和 532 nm 波长处均表现出相对更高的激光雷达比，而中东沙尘气溶胶的激光雷达比相对较低。图 5 中撒哈拉沙尘气溶胶的雷达比不确定度大于中东沙尘气溶胶和亚洲沙尘气溶胶，这可能是由于撒哈拉沙尘气溶胶的历史数据主要是远距离传输后的观测结果。在沙尘气溶胶的传输过程中，其与生物质燃烧气溶胶混合会导致观测到的激光雷达比偏大[112]，而其与海洋气溶胶混合则会导致观测到的激光雷达比较小[113]。因此在气溶胶分类时，需要考虑气溶胶源地以及传输路径的影响。

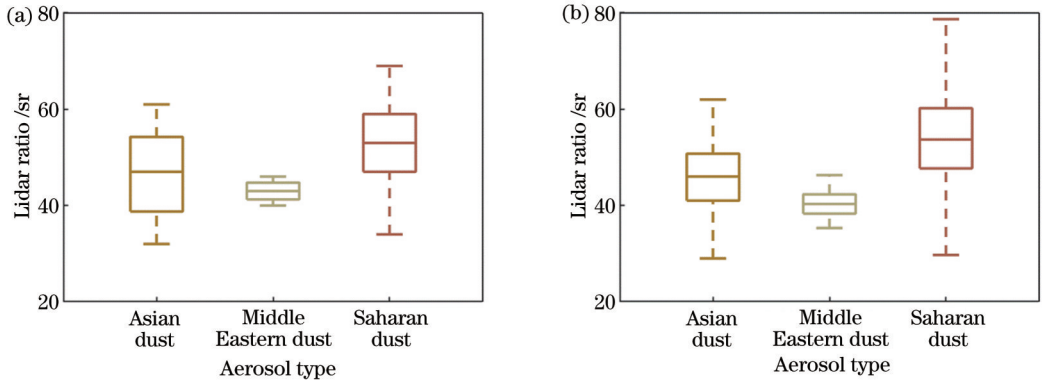

图 5　亚洲沙尘、中东沙尘、撒哈拉沙尘气溶胶在不同波长处的激光雷达比历史数据置信度分布箱图。(a) 355 nm；(b) 532 nm

Fig. 5　Distribution box diagrams of confidence level of historical lidar ratio data for Asian dust, Middle Eastern dust, and Saharan dust aerosols at different wavelengths. (a) 355 nm; (b) 532 nm

浙江大学 Liu 等[114]结合电磁理论仿真分析和历史实验观测分析，参照美国国家航空航天局兰利研究中心 Burton 等[25]对机载 HSRL 的 18 次北美洲野外观测实验的分析结果，构建了不同类型气溶胶的光学特性仿真数据库，其中包括激光雷达比。图 6 将所述 532 nm 波长处的历史数据置信度分布情况与该仿真数据库进行了对比，发现整体分布较为一致。其中：烟尘和城市气溶胶的数据分布基本一致。沙尘和海洋气溶胶的激光雷达比分布的中位数相当，范围接近。沙尘混合气溶胶的分布范围重叠较少，这可能是因为仿真数据中混合气溶胶的种类与历史数据不完全一致。历史数据存在一定的沙尘与火山灰气溶胶或烟尘气溶胶的混合，分布集中范围数值相对偏大；而仿真数据则是沙尘与海洋气溶胶或城市气溶胶的混合，范围偏小。二者分布的集中范围存在一定差异，但都分布在沙尘气溶胶附近，总体可以接受。火山灰气溶胶由于没有实验数据支撑，没有进行仿真数据的对比。

根据气溶胶激光雷达比历史数据的分析结果，将图 6 中 25%～75% 的高置信度激光雷达比范围及中值总结在表 3 中。不同类型气溶胶的激光雷达比值均存在重叠的情况，但各个类型仍有一定区分。其中：激光雷达比大于 66 sr 表明可能存在烟尘气溶胶或火山灰气溶胶，激光雷达比小于 33 sr 表明存在海洋气溶胶，沙尘、沙尘混合、城市气溶胶的激光雷达比均集中在 50～60 sr 范围内。显然，仅以激光雷达比作为气溶胶的分类指标无法很好地区分气溶胶的不同类型。因

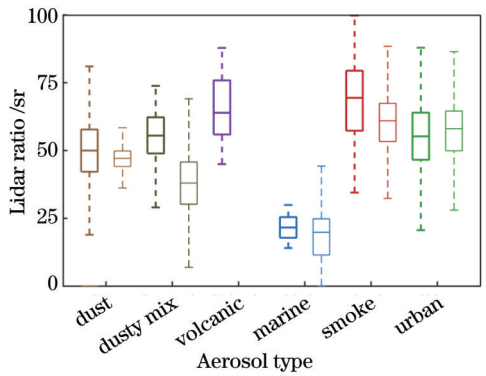

图 6　激光雷达比历史数据置信度（粗线）与仿真数据置信度（细线）对比箱图

Fig. 6　Comparison box plot of confidence level of historical lidar ratio data (thick line) and simulation data (thin line)

此，使用激光雷达进行气溶胶分类时通常需要再引入至少一个分类指标，如退偏比[21,23,114]、单次散射反照率[115]等，与激光雷达比共同作为气溶胶分类的标准。

4.4　权重选择合理性讨论

如前所述，数据代表性、可靠性、影响力三个模糊评价因子的重要性排序，即判断矩阵以及权重向量的条件为 $a_{12}<a_{13}$，$a_{23}>1$ 且 $w_1>w_2>w_3$。满足上述条件并通过 AHP 一致性检验的权重组合共计 101 组，所有权重组合的分布如图 7(a) 所示。对权重的选择基于以下原则：一是所有评价因子均能体现其意义；二是表 3 中的激光雷达比置信度较高的范围相对集中。因此，在权重向量的选择上，令权重向量的协方差 σ 以

表 3　各类气溶胶激光雷达比的高置信度范围(括号中为中值)

Table 3　High confidence level ranges of lidar ratios for all types of aerosols (the median value is in parentheses)

Type of aerosol	355 nm /sr	532 nm /sr
Dust	**43-57(49)**	**42-58(50)**
Asian dust	39-54(47)	41-51(46)
Middle Eastern dust	41-45(43)	38-42(40)
Saharan dust	47-59(53)	47-60(53)
Dusty mix	**46-62(54)**	**45-61(53)**
Volcanic	**52-68(58)**	**55-77(65)**
Marine	**22-33(28)**	**18-24(20)**
Smoke	**52-80(64)**	**53-78(68)**
Urban	**43-64(54)**	**48-66(56)**

及激光雷达比置信度箱图的箱体区间占比 q 均保持较小值。图 7(b)、(c)分别展示了在 355 nm 和 532 nm 波长处不同权重选择下协方差 σ 与箱体区间占比 q 的乘积。在 355 nm 和 532 nm 波长处所有的气溶胶类型中,第一组权重选择均能够获得最低的综合值,此时的权重向量 $\boldsymbol{W}=[w_1, w_2, w_3]=[0.54, 0.30, 0.16]$,与上述所选取值一致。

5　结　　论

激光雷达比是利用激光雷达研究气溶胶时的关键物理参数,也是气溶胶类型识别中的重要指标。在气溶胶激光雷达比的历史文献数据中,气溶胶类型的判别结果以及数值范围明确,但气溶胶类型的定义标准不统一,同一类型气溶胶的激光雷达比在不同文献中存在差异,历史文献数据分布散乱,且未见专门针对气溶胶历史文献数据的分析方法。本文基于模糊综合评价,提出了对气溶胶激光雷达比历史数据的分析方法,构造了置信度这一模糊评价指标。然后以 Web of Science 核心合集数据库中 2022 年前发表的包含气溶胶实测数据的类型判别结果共 283 条历史文献数据为例,利用数据代表性、可靠性、影响力三个评价因子对上述历史数据展开模糊评价分析,并对评价因子权重选择的合理性进行了讨论。

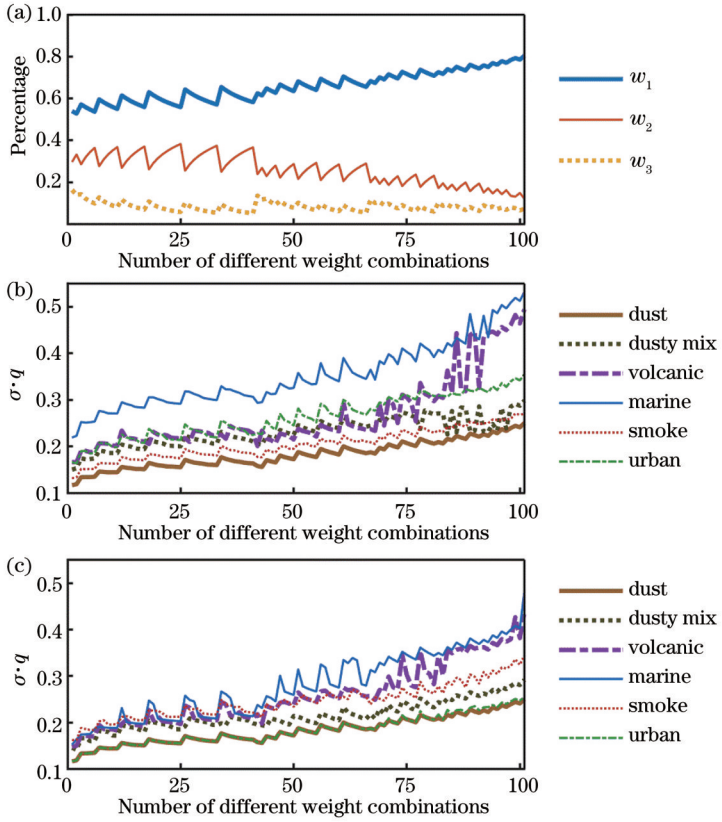

图 7　所有满足模糊综合评价法条件的权重组合结果分布。(a)所有满足重要性排序的权重组合分布;(b)不同类型气溶胶在 355 nm 波长处权重向量协方差 σ 与箱体区间占比 q 的乘积随权重选择的变化;(c)不同类型气溶胶在 532 nm 波长处权重向量协方差 σ 与箱体区间占比 q 的乘积随权重选择的变化

Fig. 7　Distribution of the results of all weight combinations satisfying the conditions of the fuzzy comprehensive evaluation method. (a) Distribution of weight combinations that meet importance ranking; (b) variation of the product of the weight vector covariance σ and the proportion of the box interval q at 355 nm wavelength for different types of aerosols with weight selection; (c) variation of the product of the weight vector covariance σ and the proportion of the box interval q at 532 nm wavelength for different types of aerosols with weight selection

模糊综合评价分析结果表明，所有类型气溶胶的激光雷达比历史数据均呈高斯分布，且当历史数据量越大时，高斯分布拟合效果越好。而传统的气溶胶类型识别方法为决策树法，该方法使用固定的阈值截断气溶胶数据，容易造成气溶胶类型的误识别以及分类不连续，且不同类型气溶胶的激光雷达比值均存在重叠的情况，仅参考激光雷达比并不能很好地区分气溶胶的不同类型，因此在进行气溶胶类型识别时需要再引入至少一个分类指标。本研究存在一些局限，如模糊综合评价的指标选择、权重确定、隶属度函数的分析等过程存在一定的主观性，但并不影响定性的分析结论。另外，本研究仅考虑了历史文献数据中的实测数据，提出的模糊综合评价分析方法在充分考虑评价指标、权重和隶属度函数等之后同样适用于气溶胶仿真数据。

丰富的历史文献数据能与气溶胶观测数据产品提供的数据形成互补，所提激光雷达比历史文献数据模糊综合分析方法有助于提升研究者对气溶胶光学特性的认识。在现有气溶胶历史数据的基础上，发展高度融合的气溶胶观测数据共享将是未来气溶胶研究的重点之一。目前，全球已经建立了多个地基气溶胶激光雷达网，我国的激光雷达网也在陆续建立或完善，如：中国科学院安徽光学精密机械研究所正在建设的“京津冀”地区激光雷达观测网、兰州大学正在建设的“一带一路”激光雷达网以及浙江大学正在筹划的“SAMENET”激光雷达网。2022 年 4 月 16 日我国成功将大气环境监测卫星发射升空，这是我国第一颗可探测全球气溶胶和云三维分布的星载激光雷达卫星[14,116]。未来丰富的地基激光雷达网和星载激光雷达观测数据将进一步推动气溶胶特性以及其辐射效应等的相关研究。

参 考 文 献

[1] Papayannis A, Balis D, Amiridis V, et al. Measurements of Saharan dust aerosols over the Eastern Mediterranean using elastic backscatter-Raman lidar, spectrophotometric and satellite observations in the frame of the EARLINET project[J]. Atmospheric Chemistry and Physics, 2005, 5(8): 2065-2079.

[2] Sun H Y, Wang S L, Hu X B, et al. Detection of surface defects and subsurface defects of polished optics with multisensor image fusion[J]. PhotoniX, 2022, 3(1): 1-14.

[3] Yu H B, Remer L A, Chin M, et al. Aerosols from overseas rival domestic emissions over North America[J]. Science, 2012, 337(6094): 566-569.

[4] Wang K Q, Zhang M M, Tang J, et al. Deep learning wavefront sensing and aberration correction in atmospheric turbulence[J]. PhotoniX, 2021, 2(1): 1-11.

[5] Wang N C, Zhang K, Shen X, et al. Dual-field-of-view high-spectral-resolution lidar: simultaneous profiling of aerosol and water cloud to study aerosol-cloud interaction[J]. Proceedings of the National Academy of Sciences of the United States of America, 2022, 119(10): e2110756119.

[6] Dubovik O, Holben B, Eck T F, et al. Variability of absorption and optical properties of key aerosol types observed in worldwide locations[J]. Journal of the Atmospheric Sciences, 2002, 59(3): 590-608.

[7] Chen S J, Tong B W, Russell L M, et al. Lidar-based daytime boundary layer height variation and impact on the regional satellite-based $PM_{2.5}$ estimate[J]. Remote Sensing of Environment, 2022, 281: 113224.

[8] Fiocco G, Smullin L D. Detection of scattering layers in the upper atmosphere (60-140 km) by optical radar[J]. Nature, 1963, 199(4900): 1275-1276.

[9] Li Y Q, Zheng W, Huang F. All-silicon photovoltaic detectors with deep ultraviolet selectivity[J]. PhotoniX, 2020, 1(1): 1-11.

[10] Fernald F G. Analysis of atmospheric lidar observations: some comments[J]. Applied Optics, 1984, 23(5): 652-653.

[11] 陈洁. 大气气溶胶消光后向散射比反演方法研究[D]. 杭州: 浙江大学, 2022.
Chen J. Study on inversion method of atmospheric aerosol extinction backscattering ratio[D]. Hangzhou: Zhejiang University, 2022.

[12] Ackermann J. The extinction-to-backscatter ratio of tropospheric aerosol: a numerical study[J]. Journal of Atmospheric and Oceanic Technology, 1998, 15(4): 1043-1050.

[13] Jiang B, Zhu S, Ren L H, et al. Simultaneous ultraviolet, visible, and near-infrared continuous-wave lasing in a rare-earth-doped microcavity[J]. Advanced Photonics, 2022, 4(4): 046003.

[14] 刘东, 陈斯婕, 刘群, 等. 星载环境探测激光雷达及其关键技术[J]. 光学学报, 2022, 42(17): 1701001.
Liu D, Chen S J, Liu Q, et al. Spaceborne environmental detection lidar and its key techniques[J]. Acta Optica Sinica, 2022, 42(17): 1701001.

[15] Jia L M, Zheng W, Huang F. Vacuum-ultraviolet photodetectors[J]. PhotoniX, 2020, 1(1): 1-25.

[16] 项衍. 激光雷达区域组网数据的三维同化与综合分析方法研究[D]. 合肥: 中国科学技术大学, 2018.
Xiang Y. Research on three-dimensional assimilation and comprehensive analysis method of lidar area network data[D]. Hefei: University of Science and Technology of China, 2018.

[17] del Rocio Camacho-Morales M, Rocco D, Xu L, et al. Infrared upconversion imaging in nonlinear metasurfaces[J]. Advanced Photonics, 2021, 3(3): 036002.

[18] Dawson K W, Meskhidze N, Josset D, et al. Spaceborne observations of the lidar ratio of marine aerosols[J]. Atmospheric Chemistry and Physics, 2015, 15(6): 3241-3255.

[19] Huang Z T, Chang C Y, Chen K P, et al. Tunable lasing direction in one-dimensional suspended high-contrast grating using bound states in the continuum[J]. Advanced Photonics, 2022, 4(6): 066004.

[20] 江高. 模糊层次综合评价法及其应用[D]. 天津: 天津大学, 2005.
Jiang G. Fuzzy hierarchical comprehensive evaluation method and its application[D]. Tianjin: Tianjin University, 2005.

[21] Wang D X, Szczepanik D, Stachlewska I S. Interrelations between surface, boundary layer, and columnar aerosol properties derived in summer and early autumn over a continental urban site in Warsaw, Poland[J]. Atmospheric Chemistry and Physics, 2019, 19(20): 13097-13128.

[22] Hamill P, Giordano M, Ward C, et al. An AERONET-based aerosol classification using the Mahalanobis distance[J]. Atmospheric Environment, 2016, 140: 213-233.

[23] Omar A H, Winker D M, Vaughan M A, et al. The CALIPSO automated aerosol classification and lidar ratio selection algorithm [J]. Journal of Atmospheric and Oceanic Technology, 2009, 26 (10): 1994-2014.

[24] Levy R C, Remer L A, Mattoo S, et al. Second-generation operational algorithm: retrieval of aerosol properties over land from inversion of Moderate Resolution Imaging Spectroradiometer spectral reflectance[J]. Journal of Geophysical Research: Atmospheres, 2007, 112(D13): D13211.

[25] Burton S P, Ferrare R A, Hostetler C A, et al. Aerosol classification using airborne high spectral resolution lidar measurements-methodology and examples[J]. Atmospheric Measurement Techniques, 2012, 5(1): 73-98.
[26] Wang Z, Liu C, Hu Q H, et al. Quantify the contribution of dust and anthropogenic sources to aerosols in North China by lidar and validated with CALIPSO[J]. Remote Sensing, 2021, 13(9): 1811.
[27] Han Y, Wu Y H, Wang T J, et al. Characterizing a persistent Asian dust transport event: optical properties and impact on air quality through the ground-based and satellite measurements over Nanjing, China[J]. Atmospheric Environment, 2015, 115: 304-316.
[28] Wang Z T, Zhang L, Cao X J, et al. Analysis of dust aerosol by using dual-wavelength lidar[J]. Aerosol and Air Quality Research, 2012, 12(4): 608-614.
[29] Hofer J, Althausen D, Abdullaev S F, et al. Long-term profiling of mineral dust and pollution aerosol with multiwavelength polarization Raman lidar at the Central Asian site of Dushanbe, Tajikistan: case studies[J]. Atmospheric Chemistry and Physics, 2017, 17(23): 14559-14577.
[30] Mamouri R E, Ansmann A, Nisantzi A, et al. Low Arabian dust extinction-to-backscatter ratio[J]. Geophysical Research Letters, 2013, 40(17): 4762-4766.
[31] Hofer J, Ansmann A, Althausen D, et al. Optical properties of Central Asian aerosol relevant for spaceborne lidar applications and aerosol typing at 355 and 532 nm[J]. Atmospheric Chemistry and Physics, 2020, 20(15): 9265-9280.
[32] Filioglou M, Giannakaki E, Backman J, et al. Optical and geometrical aerosol particle properties over the United Arab Emirates[J]. Atmospheric Chemistry and Physics, 2020, 20(14): 8909-8922.
[33] Nisantzi A, Mamouri R E, Ansmann A, et al. Middle East versus Saharan dust extinction-to-backscatter ratios[J]. Atmospheric Chemistry and Physics, 2015, 15(12): 7071-7084.
[34] Kim M H, Kim S W, Omar A H. Dust lidar ratios retrieved from the CALIOP measurements using the MODIS AOD as a constraint[J]. Remote Sensing, 2020, 12(2): 251.
[35] Hu Q Y, Wang H F, Goloub P, et al. The characterization of Taklamakan dust properties using a multiwavelength Raman polarization lidar in Kashi, China[J]. Atmospheric Chemistry and Physics, 2020, 20(22): 13817-13834.
[36] Soupiona O, Samaras S, Ortiz-Amezcua P, et al. Retrieval of optical and microphysical properties of transported Saharan dust over Athens and Granada based on multi-wavelength Raman lidar measurements: study of the mixing processes[J]. Atmospheric Environment, 2019, 214: 116824.
[37] Groß S, Freudenthaler V, Schepanski K, et al. Optical properties of long-range transported Saharan dust over Barbados as measured by dual-wavelength depolarization Raman lidar measurements[J]. Atmospheric Chemistry and Physics, 2015, 15(19): 11067-11080.
[38] Liu Z Y, Winker D, Omar A, et al. Effective lidar ratios of dense dust layers over North Africa derived from the CALIOP measurements[J]. Journal of Quantitative Spectroscopy and Radiative Transfer, 2011, 112(2): 204-213.
[39] McAuliffe M A P, Ruth A A. Typical tropospheric aerosol backscatter profiles for southern Ireland: the cork Raman lidar[J]. Atmospheric Research, 2013, 120/121: 334-342.
[40] Christine B, Stefanos S, Moritz H. Retrieval of dust microphysical properties[J]. EPJ Web of Conferences, 2020, 237: 08019.
[41] Mona L, Papagiannopoulos N, Basart S, et al. EARLINET dust observations vs. BSC-DREAM8b modeled profiles: 12-year-long systematic comparison at Potenza, Italy[J]. Atmospheric Chemistry and Physics, 2014, 14(16): 8781-8793.
[42] Soupiona O, Papayannis A, Kokkalis P, et al. EARLINET observations of Saharan dust intrusions over the northern Mediterranean region (2014-2017): properties and impact on radiative forcing[J]. Atmospheric Chemistry and Physics, 2020, 20(23): 15147-15166.
[43] Córdoba-Jabonero C, Andrey-Andrés J, Gómez L, et al. Vertical mass impact and features of Saharan dust intrusions derived from ground-based remote sensing in synergy with airborne *in situ* measurements[J]. Atmospheric Environment, 2016, 142: 420-429.
[44] Veselovskii I, Hu Q Y, Goloub P, et al. Variability in lidar-derived particle properties over West Africa due to changes in absorption: towards an understanding[J]. Atmospheric Chemistry and Physics, 2020, 20(11): 6563-6581.
[45] Wang N C, Shen X, Xiao D, et al. Development of ZJU high-spectral-resolution lidar for aerosol and cloud: feature detection and classification[J]. Journal of Quantitative Spectroscopy and Radiative Transfer, 2021, 261: 107513.
[46] Xiao D, Wang N C, Chen S J, et al. Simultaneous profiling of dust aerosol mass concentration and optical properties with polarized high-spectral-resolution lidar[J]. Science of the Total Environment, 2023, 872: 162091.
[47] Peng L, Yi F, Liu F C, et al. Optical properties of aerosol and cloud particles measured by a single-line-extracted pure rotational Raman lidar[J]. Optics Express, 2021, 29(14): 21947-21964.
[48] Hara Y, Nishizawa T, Sugimoto N, et al. Optical properties of mixed aerosol layers over Japan derived with multi-wavelength Mie-Raman lidar system[J]. Journal of Quantitative Spectroscopy and Radiative Transfer, 2017, 188: 20-27.
[49] Tesche M, Ansmann A, Müller D, et al. Particle backscatter, extinction, and lidar ratio profiling with Raman lidar in south and north China[J]. Applied Optics, 2007, 46(25): 6302-6308.
[50] Chazette P, Marnas F, Totems J. The mobile water vapor aerosol Raman lidar and its implication in the framework of the HyMeX and ChArMEx programs: application to a dust transport process[J]. Atmospheric Measurement Techniques, 2014, 7(6): 1629-1647.
[51] Haarig M, Ansmann A, Engelmann R, et al. First triple-wavelength lidar observations of depolarization and extinction-to-backscatter ratios of Saharan dust[J]. Atmospheric Chemistry and Physics, 2022, 22(1): 355-369.
[52] Kokkalis P, Soupiona O, Papanikolaou C A, et al. Radiative effect and mixing processes of a long-lasting dust event over Athens, Greece, during the COVID-19 period[J]. Atmosphere, 2021, 12(3): 318.
[53] Mamouri R E, Ansmann A, Nisantzi A, et al. Extreme dust storm over the eastern Mediterranean in September 2015: satellite, lidar, and surface observations in the Cyprus region[J]. Atmospheric Chemistry and Physics, 2016, 16(21): 13711-13724.
[54] Royer P, Chazette P, Lardier M, et al. Aerosol content survey by mini N2-Raman lidar: application to local and long-range transport aerosols[J]. Atmospheric Environment, 2011, 45(39): 7487-7495.
[55] Wang H F, Li Z Q, Goloub P, et al. Identification of typical dust sources in Tarim Basin based on multi-wavelength Raman polarization lidar[J]. Atmospheric Environment, 2022, 290: 119358.
[56] Wang S H, Lei H W, Pani S K, et al. Determination of lidar ratio for major aerosol types over western North Pacific based on long-term MPLNET data[J]. Remote Sensing, 2020, 12(17): 2769.
[57] Zhang S, Huang Z W, Li M S, et al. Vertical structure of dust aerosols observed by a ground-based Raman lidar with polarization capabilities in the center of the Taklimakan Desert [J]. Remote Sensing, 2022, 14(10): 2461.
[58] Rittmeister F, Ansmann A, Engelmann R, et al. Profiling of

Saharan dust from the Caribbean to western Africa-part1: layering structures and optical properties from shipbornepolarization/Raman lidar observations[J]. Atmospheric Chemistry and Physics, 2017, 17(21): 12963-12983.

[59] Veselovskii I, Goloub P, Podvin T, et al. Characterization of smoke and dust episode over West Africa: comparison of MERRA-2 modeling with multiwavelength Mie-Raman lidar observations[J]. Atmospheric Measurement Techniques, 2018, 11(2): 949-969.

[60] Mylonaki M, Papayannis A, Anagnou D, et al. Optical and microphysical properties of aged biomass burning aerosols and mixtures, based on 9-year multiwavelength Raman lidar observations in Athens, Greece[J]. Remote Sensing, 2021, 13 (19): 3877.

[61] Ancellet G, Pelon J, Totems J, et al. Long-range transport and mixing of aerosol sources during the 2013 North American biomass burning episode: analysis of multiple lidar observations in the western Mediterranean Basin[J]. Atmospheric Chemistry and Physics, 2016, 16(7): 4725-4742.

[62] Groß S, Gasteiger J, Freudenthaler V, et al. Saharan dust contribution to the Caribbean summertime boundary layer-a lidar study during SALTRACE[J]. Atmospheric Chemistry and Physics, 2016, 16(18): 11535-11546.

[63] Engelmann R, Haarig M, Baars H, et al. Measurements of particle backscatter, extinction, and lidar ratio at 1064 nm with the rotational raman method in polly-XT[J]. EPJ Web of Conferences, 2018, 176: 01004.

[64] Saha S, Sharma S, Kumar K N, et al. A case study on the vertical distribution and characteristics of aerosols using ground-based Raman lidar, satellite and model over Western India[J]. International Journal of Remote Sensing, 2021, 42(17): 6417-6432.

[65] Papayannis A, Nicolae D, Kokkalis P, et al. Optical, size and mass properties of mixed type aerosols in Greece and Romania as observed by synergy of lidar and sunphotometers in combination with model simulations: a case study[J]. Science of the Total Environment, 2014, 500/501: 277-294.

[66] Wang Z, Liu C, Dong Y S, et al. Profiling of dust and urban haze mass concentrations during the 2019 national day parade in Beijing by polarization Raman lidar[J]. Remote Sensing, 2021, 13(16): 3326.

[67] Groß S, Freudenthaler V, Wiegner M, et al. Dual-wavelength linear depolarization ratio of volcanic aerosols: lidar measurements of the Eyjafjallajökull plume over Maisach, Germany[J]. Atmospheric Environment, 2012, 48: 85-96.

[68] Klekociuk A R, Ottaway D J, MacKinnon A D, et al. Australian lidar measurements of aerosol layers associated with the 2015 calbuco eruption[J]. Atmosphere, 2020, 11(2): 124.

[69] Prata A T, Young S A, Siems S T, et al. Lidar ratios of stratospheric volcanic ash and sulfate aerosols retrieved from CALIOP measurements[J]. Atmospheric Chemistry and Physics, 2017, 17(13): 8599-8618.

[70] Mortier A, Goloub P, Podvin T, et al. Detection and characterization of volcanic ash plumes over Lille during the Eyjafjallajökull eruption[J]. Atmospheric Chemistry and Physics, 2013, 13(7): 3705-3720.

[71] Kokkalis P, Papayannis A, Amiridis V, et al. Optical, microphysical, mass and geometrical properties of aged volcanic particles observed over Athens, Greece, during the Eyjafjallajökull eruption in April 2010 through synergy of Raman lidar and sunphotometer measurements[J]. Atmospheric Chemistry and Physics, 2013, 13(18): 9303-9320.

[72] Ansmann A, Tesche M, Groß S, et al. The 16 April 2010 major volcanic ash plume over central Europe: EARLINET lidar and AERONET photometer observations at Leipzig and Munich, Germany[J]. Geophysical Research Letters, 2010, 37 (13): L13810.

[73] Pisani G, Boselli A, Coltelli M, et al. Lidar depolarization measurement of fresh volcanic ash from Mt. Etna, Italy[J]. Atmospheric Environment, 2012, 62: 34-40.

[74] Lopes F, Silva J, Marrero J, et al. Synergetic aerosol layer observation after the 2015 Calbuco volcanic eruption event[J]. Remote Sensing, 2019, 11(2): 195.

[75] Chouza F, Leblanc T, Barnes J, et al. Long-term (1999-2019) variability of stratospheric aerosol over Mauna Loa, Hawaii, as seen by two co-located lidars and satellite measurements[J]. Atmospheric Chemistry and Physics, 2020, 20(11): 6821-6839.

[76] Haarig M, Ansmann A, Gasteiger J, et al. Dry versus wet marine particle optical properties: RH dependence of depolarization ratio, backscatter, and extinction from multiwavelength lidar measurements during SALTRACE[J]. Atmospheric Chemistry and Physics, 2017, 17(23): 14199-14217.

[77] Guerrero-Rascado J L, Andrey J, Sicard M, et al. Aerosol closure study by lidar, Sun photometry, and airborne optical counters during DAMOCLES field campaign at El Arenosillo sounding station, Spain[J]. Journal of Geophysical Research: Atmospheres, 2011, 116(D2): D02209.

[78] Wang L L, Stanič S, Eichinger W, et al. Investigation of aerosol properties and structures in two representative meteorological situations over the Vipava valley using polarization Raman LiDAR[J]. Atmosphere, 2019, 10(3): 128.

[79] Floutsi A A, Baars H, Radenz M, et al. Advection of biomass burning aerosols towards the southern hemispheric mid-latitude station of Punta Arenas as observed with multiwavelength polarization Raman lidar[J]. Remote Sensing, 2021, 13(1): 138.

[80] Ohneiser K, Ansmann A, Baars H, et al. Smoke of extreme Australian bushfires observed in the stratosphere over Punta Arenas, Chile, in January 2020: optical thickness, lidar ratios, and depolarization ratios at 355 and 532 nm[J]. Atmospheric Chemistry and Physics, 2020, 20(13): 8003-8015.

[81] Lopes F J S, Moreira G A, Rodrigues P F, et al. Lidar measurements of tropospheric aerosol and water vapor profiles during the winter season campaigns over the metropolitan area of São Paulo, Brazil[J]. Proceedings of SPIE, 2014, 9246: 92460H.

[82] Stachlewska I, Samson M, Zawadzka O, et al. Modification of local urban aerosol properties by long-range transport of biomass burning aerosol[J]. Remote Sensing, 2018, 10(3): 412.

[83] Haarig M, Ansmann A, Baars H, et al. Depolarization and lidar ratios at 355, 532, and 1064 nm and microphysical properties of aged tropospheric and stratospheric Canadian wildfire smoke[J]. Atmospheric Chemistry and Physics, 2018, 18(16): 11847-11861.

[84] Ritter C, Burgos M A, Böckmann C, et al. Microphysical properties and radiative impact of an intense biomass burning aerosol event measured over Ny-Ålesund, Spitsbergen in July 2015[J]. Tellus B: Chemical and Physical Meteorology, 2018, 70(1): 1539618.

[85] Ohneiser K, Ansmann A, Chudnovsky A, et al. The unexpected smoke layer in the High Arctic winter stratosphere during MOSAiC 2019-2020[J]. Atmospheric Chemistry and Physics, 2021, 21(20): 15783-15808.

[86] Baars H, Radenz M, Floutsi A A, et al. Californian wildfire smoke over Europe: a first example of the aerosol observing capabilities of Aeolus compared to ground-based lidar[J]. Geophysical Research Letters, 2021, 48(8): e2020GL092194.

[87] Hu Q Y, Goloub P, Veselovskii I, et al. The characterization of long-range transported North American biomass burning plumes: what can a multi-wavelength Mie-Raman-polarization-fluorescence lidar provide? [J]. Atmospheric Chemistry and Physics, 2022, 22(8): 5399-5414.

[88] de Arruda Moreira G, da Silva Andrade I, Cacheffo A, et al. Influence of a biomass-burning event in $PM_{2.5}$ concentration and

air quality: a case study in the metropolitan area of São Paulo[J]. Sensors, 2021, 21(2): 425.

[89] Wu Y H, Nehrir A R, Ren X R, et al. Synergistic aircraft and ground observations of transported wildfire smoke and its impact on air quality in New York City during the summer 2018 LISTOS campaign[J]. Science of the Total Environment, 2021, 773: 145030.

[90] Vaughan G, Draude A P, Ricketts H M A, et al. Transport of Canadian forest fire smoke over the UK as observed by lidar[J]. Atmospheric Chemistry and Physics, 2018, 18(15): 11375-11388.

[91] Haarig M, Baars H, Ansmann A, et al. Wildfire smoke in the stratosphere over Europe-first measurements of depolarization and lidar ratios at 355, 532, and 1064 nm[J]. EPJ Web of Conferences, 2020, 237: 02036.

[92] Wang X, Boselli A, He Y, et al. Urban aerosol optical properties measurement by elastic counter-look lidar[J]. EPJ Web of Conferences, 2016, 119: 23029.

[93] Radhakrishnan S R, Singh S K, Sharma C, et al. Initial assessment of lidar signal and the first result of a Raman lidar installed at a high altitude station in India[J]. Remote Sensing Applications: Society and Environment, 2020, 18: 100309.

[94] Groß S, Esselborn M, Abicht F, et al. Airborne high spectral resolution lidar observation of pollution aerosol during EUCAARI-LONGREX[J]. Atmospheric Chemistry and Physics, 2013, 13(5): 2435-2444.

[95] Wang W, Gong W, Mao F Y, et al. Measurement and study of lidar ratio by using a Raman lidar in central China[J]. International Journal of Environmental Research and Public Health, 2016, 13(5): 508.

[96] Ansmann A, Wagner F, Althausen D, et al. European pollution outbreaks during ACE 2: lofted aerosol plumes observed with Raman lidar at the Portuguese coast[J]. Journal of Geophysical Research: Atmospheres, 2001, 106(D18): 20725-20733.

[97] Hee W S, Lim H S, Jafri M Z M, et al. Vertical profiling of aerosol types observed across monsoon seasons with a Raman lidar in Penang Island, Malaysia[J]. Aerosol and Air Quality Research, 2016, 16(11): 2843-2854.

[98] Chen Z Y, Liu W Q, Heese B, et al. Aerosol optical properties observed by combined Raman-elastic backscatter lidar in winter 2009 in Pearl River Delta, South China[J]. Journal of Geophysical Research: Atmospheres, 2014, 119(5): 2496-2510.

[99] Wang B Y, Liu D, Pan S Q, et al. High-spectral-resolution LIDAR based on a few-longitudinal mode laser for aerosol and cloud characteristics detection[J]. Optics Letters, 2022, 47(19): 5028-5031.

[100] Kok J F, Ridley D A, Zhou Q, et al. Smaller desert dust cooling effect estimated from analysis of dust size and abundance [J]. Nature Geoscience, 2017, 10(4): 274-278.

[101] Zhang R Y, Wang G H, Guo S, et al. Formation of urban fine particulate matter[J]. Chemical Reviews, 2015, 115(10): 3803-3855.

[102] Mather T A, Allen A G, Oppenheimer C, et al. Size-resolved characterisation of soluble ions in the particles in the tropospheric plume of masaya volcano, Nicaragua: origins and plume processing[J]. Journal of Atmospheric Chemistry, 2003, 46(3): 207-237.

[103] Raes F, Van Dingenen R, Vignati E, et al. Formation and cycling of aerosols in the global troposphere[J]. Atmospheric Environment, 2000, 34(25): 4215-4240.

[104] Rinaldi M, Decesari S, Finessi E, et al. Primary and secondary organic marine aerosol and oceanic biological activity: recent results and new perspectives for future studies[J]. Advances in Meteorology, 2010, 2010: 310682.

[105] Pisani G, Armenante M, Boselli A, et al. Atmospheric aerosol characterization during Saharan dust outbreaks at Naples EARLINET station[J]. Proceedings of SPIE, 2007, 6745: 67451R.

[106] Noh Y M, Kim Y J, Choi B C, et al. Aerosol lidar ratio characteristics measured by a multi-wavelength Raman lidar system at Anmyeon Island, Korea[J]. Atmospheric Research, 2007, 86(1): 76-87.

[107] Herrera M E, Dubovik O, Torres B, et al. Estimates of remote sensing retrieval errors by the GRASP algorithm: application to ground-based observations, concept and validation[J]. Atmospheric Measurement Techniques, 2022, 15(20): 6075-6126.

[108] Kim M H, Omar A H, Tackett J L, et al. The CALIPSO version 4 automated aerosol classification and lidar ratio selection algorithm[J]. Atmospheric Measurement Techniques, 2018, 11 (11): 6107-6135.

[109] Ansmann A, Wandinger U, Riebesell M, et al. Independent measurement of extinction and backscatter profiles in cirrus clouds by using a combined Raman elastic-backscatter lidar[J]. Applied Optics, 1992, 31(33): 7113-7131.

[110] de Tomasi F, Perrone M R. Lidar measurements of African dust outbreaks[J]. Proceedings of SPIE, 2003, 4882: 400-407.

[111] Cordoba-Jabonero C, Sabbah I, Sorribas M, et al. Saharan and arabian dust aerosols: a comparative case study of lidar ratio [C]// 27th International Laser Radar Conference (ILRC), July 05-10, 2015, City University of New York, City Coll, Natl. Ocean & Atmospher Adm., Cooperat Remote Sensing Sci. & Technol. Ctr, New York, 2016: 119.

[112] Cordoba-Jabonero C, Adame J A, Campbell J R, et al. Lidar ratio derived for pure dust aerosols: multi-year micro pulse lidar observations in a saharan dust-influenced region[J]. EPJ Web of Conferences, 2016, 119: 23017.

[113] Mona L, Amodeo A, D′Amico G, et al. Five years of lidar ratio measurements over Potenza, Italy[J]. Proceedings of SPIE, 2006, 6367: 636702.

[114] Liu D, Yang Y Y, Zhang Y P, et al. Pattern recognition model for aerosol classification with atmospheric backscatter lidars: principles and simulations[J]. Journal of Applied Remote Sensing, 2015, 9(1): 096006.

[115] 周妹, 常建华, 陈思成, 等. 一种基于朴素贝叶斯分类器的气溶胶类型识别模型[J]. 光学学报, 2022, 42(18): 1801006.
Zhou M, Chang J H, Chen S C, et al. Aerosol type recognition model based on naive Bayesian classifier[J]. Acta Optica Sinica, 2022, 42(18): 1801006.

[116] Ke J, Sun Y S, Dong C Z, et al. Development of China's first space-borne aerosol-cloud high-spectral-resolution lidar: retrieval algorithm and airborne demonstration[J]. PhotoniX, 2022, 3(1): 1-20.

Fuzzy Comprehensive Evaluation of Historical Lidar Ratio Data

Hu Xianzhe[1,2], Liu Dong[1,2,3,4*], Xiao Da[1], Zhang Kai[1], Bi Lei[5], Zhang Jingxin[1], Li Weize[1], Li Xiaotao[1], Deng Jiesong[1], Zhou Yudi[1,6], Liu Qun[1,6], Wu Lan[1], Liu Chong[1], Wan Xueping[7], Chen Wentai[7], Chen Xiaolong[7], Zhou Jianfeng[7]

[1]*State Key Laboratory of Extreme Photonics and Instrumentation, College of Optical Science and Engineering, Zhejiang University, Hangzhou* 310027, *Zhejiang, China*;

[2]*Donghai Laboratory, Zhoushan* 316021, *Zhejiang, China*;

[3]*ZJU-Hangzhou Global Scientific and Technological Innovation Center, Hangzhou* 311200, *Zhejiang, China*;

[4]*Jiaxing Research Institute, Zhejiang University, Jiaxing* 314000, *Zhejiang, China*;

[5]*Key Laboratory of Geoscience Big Data and Deep Resource of Zhejiang Province, School of Earth Sciences, Zhejiang University, Hangzhou* 310027, *Zhejiang, China*;

[6]*Ningbo Innovation Center, Zhejiang University, Ningbo* 315100, *Zhejiang, China*;

[7]*Wuxi Zhongke Optoelectronic Technology Co., Ltd., Wuxi* 214135, *Jiangsu, China*

Abstract

Objective Aerosols are one of the major uncertain sources in radiative forcing assessments of the land-atmosphere system, and aerosol profile data detected by lidar can help quantitatively assess the climate effects of aerosols. In addition to published aerosol observation products, a large amount of aerosol lidar observation data are distributed in the references. However, there is still a lack of integrated analysis of historical aerosol reference data. Thus, we focus on the lidar ratio parameters that are relatively lacking in the existing observation products and propose a fuzzy comprehensive evaluation and analysis method of historical lidar ratio data with aerosol type differences fully considered. The historical data can complement the products of aerosol observation data, and the proposed evaluation and analysis method can help improving the understanding of optical aerosol properties.

Methods Based on the idea of fuzzy comprehensive evaluation, we propose a fuzzy comprehensive evaluation and analysis method for the historical reference data of aerosol lidar ratio, and design the evaluation index of confidence level. The confidence level analysis is shown in Fig. 1. First, the evaluation factors of the historical data are selected, and the analytic hierarchy process (AHP) is employed to determine the contribution proportion of each evaluation factor to the confidence level. Then, according to the characteristics of these factors, the membership function of each factor is determined, and the contribution weights are multiplied by the membership function to get the confidence value. Finally, the confidence values of all historical data are calculated, and the historical data of the same type and wavelength are accumulated to obtain the distribution of the total confidence values of the lidar ratio. To enable comparative evaluation, we normalize the total confidence values to obtain the distribution of confidence level for different types of aerosols lidar ratio over historical data.

Results and Discussions All observations of aerosol lidar ratios in the Web of Science database are analyzed with confidence level by the proposed evaluation method. We find that all aerosol types show different aggregation trends similar to Gaussian distribution on the lidar ratio distribution, and the larger amount of historical data lead to a better Gaussian fitting effect. Additionally, the analysis is carried out for sand and dust aerosols from different sources, and the results shown in Fig. 5 indicate that the optical properties of the same aerosol will be different for different sources. Finally, the confidence ranges of the lidar ratios for various aerosol types are summarized in Table 3 for reference, and the results are compared with the simulation data in Fig. 6 with good consistency.

Conclusions We propose a fuzzy comprehensive evaluation and analysis method for the historical reference data of aerosol lidar ratios, which makes up for the analysis method gap of historical aerosol data and provides references for analyzing the aerosol research basis. Analysis of all the relevant observations in the Web of Science database show that the historical data of lidar ratios of all aerosol types have Gaussian distributions. The traditional aerosol type recognition method is the decision tree, which adopts a fixed threshold to truncate the aerosol data and is prone to cause aerosol type misidentification and discontinuous classification limitation. The lidar ratios of different aerosol types overlap, and they alone are unable to differentiate various aerosol types. Therefore, at least one more classification index should be introduced when aerosol type identification is needed. We present a more comprehensive historical data analysis of the aerosol lidar ratio to improve the understanding of optical aerosol properties and refine the aerosol classification results, providing an accurate reference basis for data analysis of on-board lidars.

Key words aerosol; lidar ratio; historical data; fuzzy comprehensive evaluation